

Nonadiabatic molecular dynamics simulation for carrier transport in a pentathiophene butyric acid monolayer

Junfeng Ren,^{1,2} Nenad Vukmirović,³ and Lin-Wang Wang^{1,*}

¹*Materials Sciences Division, Lawrence Berkeley National Laboratory, One Cyclotron Road, Mail Stop 66, Berkeley, California 94720, USA*

²*College of Physics and Electronics, Shandong Normal University, Jinan 250014, China*

³*Scientific Computing Laboratory, Institute of Physics Belgrade, University of Belgrade, Pregrevica 118, 11080 Belgrade, Serbia*

(Received 29 December 2012; published 13 May 2013)

We present a large-scale nonadiabatic molecular dynamics simulation to study carrier transport in an organic monolayer. This simulation calculates a 4802-atom system for 825 fs in about 3 h using 51 744 computer cores, while deploying a plane-wave pseudopotential density-functional theory Hamiltonian. A new approach is developed that makes such large-scale calculation possible. Our simulation on the pentathiophene butyric acid monolayer reveals the mechanism for the carrier transport in the system: the hole wave functions are localized by thermal fluctuation-induced disorder, while the hole transport is via charge transfer during state energy crossing. The simulation also shows that the system is never in a thermodynamic equilibrium in terms of adiabatic-state populations according to Boltzmann distribution.

DOI: [10.1103/PhysRevB.87.205117](https://doi.org/10.1103/PhysRevB.87.205117)

PACS number(s): 72.10.Bg, 73.50.Bk

I. INTRODUCTION

Carrier transport in an organic system is a complex phenomenon that can involve different underlying mechanisms.^{1,2} These include: delocalized bulk band transport,^{3,4} disorder-induced localized state hopping,⁵ atomic relaxation-induced polaron state hopping,^{6,7} polaron band structure transport,⁸ thermofluctuation-induced dynamic-disorder transport,^{9,10} and tunneling transport.^{11,12} These mechanisms give rise to rich phenomena in terms of temperature, carrier density, and electric-field dependences of the carrier mobility.^{2,13,14} Traditionally, different models are used to describe various carrier-transport phenomena in a variety of systems. However, it is not always known *a priori* which mechanism is involved for a given system. It is also possible that several mechanisms are all at work at the same time or that they dominate at different temperature regimes for the same system. Thus, it will be useful to treat all these mechanisms under a unified framework. One such approach is nonadiabatic molecular dynamics (MD) simulation.^{15–17}

Nonadiabatic MD has a long history in quantum chemistry,^{18,19} it is as old as Born-Oppenheimer MD (BO-MD).^{20,21} There are many ways to carry out nonadiabatic MD. In its most rigorous form, both the electron and nuclear degrees of freedom are described quantum mechanically by a combined wave function, and the evolution of this wave function is determined by its time-dependent Schrödinger equation. However, this approach is only possible for very small molecular systems. A common approximation for a large system is to decompose the wave function into its electronic part and nuclear part. The nuclear wave function can be approximated by frozen Gaussian wave functions as in a harmonic oscillator.²² A further approximation is to treat the nuclear movement classically using Newton's second law, while treating the electronic movement quantum mechanically following the time-dependent Schrödinger equation. This is often called the “classical path” method²³ or “mixed quantum-classical” (MQC) method.²⁴ This approximation is particularly useful to study the carrier transport where the focus is on the electronic movement, which is described quantum mechanically. This is the approach adopted in the current work.

Although our work is focused on electronic movement, a major concern in traditional MQC methodology development is to deal with the branching of nuclear dynamics caused by its couplings to different electronic states. Reversely, this branching in nuclear trajectory also causes different electronic adiabatic states to dephase from each other (losing their abilities to couple with each other coherently). Such a phenomenon is natural in a full quantum-mechanical treatment, including both the electronic and nuclear degrees of freedom. But in the MQC approach, they must be added empirically. Different approximations have been used to deal with this problem. The simplest method is to ignore such branching. This is Ehrenfest dynamics, a mean-field treatment for electronic feedback to the nuclear movement. In Ehrenfest dynamics, the electron wave function follows the time-dependent Schrödinger equation, and the resulting total energy and nuclear force are used to move the nuclei.²⁵ One straightforward way to introduce branching and decoherence is to introduce wave-function collapse in a stochastic fashion.²⁴ During wave-function collapse, the wave function instantaneously changes into one of the adiabatic states on which it has some amplitude.²⁴ However, a more popular method is the potential energy surface hopping method introduced by Tully.²⁶ In Tully's fewest-switches surface hopping (FSSH) algorithm, the nuclei move on one adiabatic energy surface (corresponding to one-electron adiabatic wave function) until a stochastic sudden hopping event knocks the system from the current adiabatic energy surface to another adiabatic energy surface. Meanwhile, an auxiliary electron wave function is calculated following the time-dependent Schrödinger equation and is decomposed into a linear combination of many adiabatic electron states. The transition rate of this auxiliary wave function from one adiabatic state to another is used to guide the probability of surface hopping.²⁶ The FSSH algorithm does introduce branching in the nuclear dynamics but does not fully solve the dephasing problem of the electronic states.^{27,28} How to deal with the dephasing and branching under the MQC framework is an intensely studied topic at the present. However, in this work, our focus is on how to numerically carry out the existing schemes for large systems, instead of researching the schemes themselves. We will use

Ehrenfest dynamics and FSSH as our examples. Nevertheless, modifications will be introduced, so they can be used to study the carrier-transport problems in hand.

Nonadiabatic MD has been used extensively to study different phenomena in quantum chemistry. It was first used to study molecule collision and scattering.²⁹ It has also been used to analyze the conical intersections of potential energy surfaces,³⁰ to simulate molecular photodissociation,³¹ to study the photoisomerization of retinal,³² and to determine the effects of charge transfer to the ionic movements in a catalytic process.³³ While some quantum chemistry calculations involve relatively small molecules, nonadiabatic MD has also been used to study extended systems, e.g., coherent or semicoherent processes,¹¹ charge transfer in a solvent,³⁴ or dynamic behavior in multielectron systems.³⁵ Recently, nonadiabatic MD was used to study nanostructure materials, e.g., carrier cooling from high excited states³⁶ and charge transfer between organic and inorganic systems.^{37,38} We also saw a recent surge in use of this method to study carrier mobility in extended organic systems.^{39–43} Studying such problems requires the use of relatively large systems (e.g., a few thousand atoms), and a long simulation time (e.g., a few picoseconds). Unfortunately, nonadiabatic MD simulation can be extremely expensive. Due to the small mass of the electron, the time step one can use to evolve the time-dependent Schrödinger equation is typically 1 as (10^{-3} fs). This is 1000 times shorter than the traditional BO-MD step for the nuclear movement. As a result, current nonadiabatic MD simulations are either for relatively small systems (e.g., less than 200 atoms),^{36–38} or for tight-binding³⁹ and other simplified Hamiltonians.^{32,44,45} The large system size also brings in other challenges. For example, there could be many energy-surface anticrossings (avoided crossings) within a given time period or energy window, and small anticrossing gaps (due to small coupling between spatially faraway states). Such rapid anticrossing and complicated energy-surface structures require much smaller time steps compared with small molecular systems. Thus, the challenges facing nonadiabatic MD for large-systems can be quite different from the ones for small molecular systems (e.g., for chemical reactions).

In this paper, we will focus on using an approach, named as the nonadiabatic MD based on the charge-patching method (NAMD-CPM), to study carrier transport for large systems. The focus is on the electronic movement, not the nuclear movement. We will ignore the electron to nuclear “back reaction.” When such back reaction is ignored, the NAMD-CPM can no longer be used to describe the polaron-based transport. But as we will discuss later, such a polaron effect is small in our system. We will focus on the special challenges for the large system simulations, e.g., the attosecond time step (due to dense state anticrossings and possible weak couplings between states). The purposes and the main contributions of this paper are twofold: (1) to introduce a linear time dependence of the Hamiltonian, which allows the increase of the time step from attosecond to femtosecond. Combining this approximation with other fast electronic structure calculation techniques, a 4802-atom system can be simulated for about 1 ps under a plane-wave pseudopotential Hamiltonian; (2) the simulation result of a monolayer of a five-thiophene-ring oligomer pentathiophene butyric acid (5TBA) reveals an interesting mechanism for the carrier transport in this system:

a thermal fluctuation-induced wave-function localization, and a charge transfer during state energy anticrossing.

II. THE FORMALISM: TIME INTEGRATION AND THE RELATED APPROXIMATIONS

There are many different ways to carry out a nonadiabatic MD; it will be useful to lay out the approaches and approximations we will use in the current work. (1) We will use an MQC method (also called the classical path method) to perform nuclear dynamics. (2) We will further decouple the nuclear dynamics from the electron quantum-mechanical dynamics (e.g., ignore the back reaction from the electronic system to the nuclear classical system), and we will use a classical force field to carry out the nuclear dynamics. The justification of this approach for the studied system will be given later. (3) Due to the lack of back reaction as described in (2), both Tully’s method and Ehrenfest dynamics have been modified, with the details given later. Nevertheless, the surface hopping in Tully’s algorithm can still provide a way to describe the populations of the system on different electronic adiabatic states. Alternatively, the electron movement can be described directly by the wave functions in Ehrenfest dynamics. However, we will introduce a modified Ehrenfest (ME) dynamics to correct a detailed balance problem in the original algorithm. (4) Our electronic system will be described by density-functional theory (DFT)⁴⁶ using a plane-wave basis under the nonlocal pseudopotential formalism. Thus, in a sense our electron dynamics is like the time-dependent DFT (TDDFT) simulation.⁴⁷ However, while in common TDDFT simulations all the electrons can be excited (e.g., under an external electric field), here we will only consider a situation in which one extra carrier is excited. More specifically, in our case, a one hole state will be excited and be distributed among many valence-band (VB) states [e.g., the hole is not just at the highest-energy VB maximum (VBM) state], and the rest of the electronic system (which is the N -electron closed-shell system) remains in its ground state (Born-Oppenheimer state) at any given time. Thus, our electron wave function in the time-dependent Schrödinger equation will be the Kohn-Sham single-particle orbital, rather than the many-body all electron wave function. Nevertheless, each single-particle adiabatic state (orbital) will correspond to one adiabatic energy surface of the whole system (when the excited carrier occupies this orbital). In the current study, we will deal with the excited hole. We will use local-density approximation (LDA)⁴⁶ as our DFT functional. Although LDA can have large errors in describing material band gaps, the hole transport only depends on the relative energies between different valence orbitals, which can be described accurately by LDA.

We will describe here the basic formalism for our NAMD-CPM simulation. Although most of these formalisms can be found elsewhere,²⁶ it is beneficial to list them out here to facilitate later discussions. If we use $\{R(t)\}$ to denote nuclear positions, which changes as a function of time t , then the single-electron Hamiltonian H , which depends on $R(t)$, is also a function of time. As a result, we have a time-dependent Schrödinger equation for the single excited hole orbital ψ as

$$i \frac{\partial \psi}{\partial t} = H(t) \psi. \quad (1)$$

Meanwhile, the MD movement of $\{R(t)\}$ is described by the classical Newton's equation:

$$M_j \frac{d^2 R_j(t)}{dt^2} = F_j. \quad (2)$$

Here, M_j is the mass of atom j , $R_j(t)$ is its position, and F_j is the force acting on atom j . The force can be calculated *ab initio* from DFT total energy based on $H(t)$. In that case, the forces depend on the single-hole wave functions ψ ; thus, Eqs. (1) and (2) are fully coupled. As mentioned above, in the current work we will use a classical force-field model to describe the nuclear movements of the organic systems. As a result, F_j only depends on the atomic configuration $\{R(t)\}$; thus, while Eq. (1) depends on Eq. (2), Eq. (2) no longer depends on Eq. (1), and it is integrated by itself (no back reaction, and we call this detachment approximation). The justification of this detachment approximation for the problems under consideration is given in Appendix A.

To solve Eq. (1), one can just apply H directly to wave function ψ at every time step. But that can be quite time consuming. Furthermore, as we will show later, it is necessary to introduce energy surface hopping or other state transition concepts. This requires us to analyze the wave function in terms of the adiabatic states (orbitals) $\{\varphi_i(t)\}$, which are eigenstates of $H(t)$ at any given time t :

$$H(t)\varphi_i(t) = \varepsilon_i(t)\varphi_i(t). \quad (3)$$

Here, for hole orbitals, the index i will begin from one starting from the VBM state. Thus $i = 1$ means the VBM state, and $i = 2$ means the VBM-1 state, and so on. A common practice to integrate Eq. (1) is to expand the wave function $\psi(t)$ using the adiabatic states:²⁶

$$\psi(t) = \sum_i C_i(t)\varphi_i(t). \quad (4)$$

Then, the solution of Eq. (1) becomes the solution of coefficients $\{C_i(t)\}$. One can plug Eq. (4) back to Eq. (1), then we have

$$\dot{C}_i(t) = -i\varepsilon_i(t)C_i(t) - \sum_k C_k(t)V_{ik}(t), \quad (5)$$

and here V_{ik} is a coupling between adiabatic states “ i ” and “ k ,” which can be calculated as²⁶

$$V_{ik}(t) = [(\varphi_i(t)|\varphi_k(t + \delta t)) - \delta_{i,k}]/\delta t \quad (6)$$

for small δt . The LDA Hamiltonian $H(t)$ in Eqs. (1) and (3) depends on atomic positions $\{R(t)\}$, the N -electron system ground-state charge density $\rho_0(t)$, and the single-hole wave functions $\psi(t)$. Here, N is the number of electrons for the closed-shell system (without the hole). Thus, for the simulated system where one hole exists, the total number of electrons is $N-1$, and the total electron charge density equals $\rho(t) = \rho_0(t) - |\psi(t)|^2$. Here comes an interesting question: whether one should use the N -electron closed-shell charge density $\rho_0(t)$, or the $N-1$ electron open-shell charge density $\rho(t)$ to derive the LDA Hamiltonian $H(t)$ in the Kohn-Sham equation of Eq. (1). If strict LDA formalism is applied, then $\rho(t)$ should be used. However, it is found that it is more accurate to use $\rho_0(t)$ instead of $\rho(t)$ to derive $H(t)$. Doing so will avoid the erroneous self-interaction problem in LDA and make the

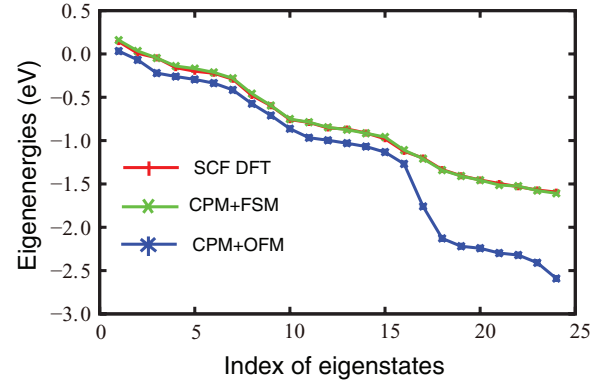


FIG. 1. (Color online) Comparison of the eigenenergies between SCF DFT, the CPM, and the CPM solved with OFM. Note the FSM is an exact method that involves no approximation for solving the electron eigenstates for a given H .

LDA Kohn-Sham equation more close to the many-body GW equation. A more detail discussion of this point is provided in Appendix B. Thus, in this work, we will use $\rho_0(t)$.

To obtain the BO ground-state charge density $\rho_0(t)$, one could occupy all the valence adiabatic states $\{\varphi_i(t)\}$ from Eq. (3) and solve the Hamiltonian H self-consistently as in a traditional BO-MD. Here, we will use the CPM^{48,49} to obtain $\rho_0(t)$ for a given atomic configuration $\{R(t)\}$. The CPM^{48,49} is a well-tested method to provide ground-state electron charge density without going through a self-consistent calculation. It generates atomic charge-density motifs from small-system calculations and then patches these motifs together to obtain the charge density of a large system. After $\rho_0(t)$ is obtained, it will be used with the LDA formalism to acquire the single particle Hamiltonian $H(t)$. The eigenenergy error of a CPM is typically 20–30 meV compared with the direct LDA calculation.⁴⁹ Figure 1 shows the comparison between the CPM and the direct self-consistent field (SCF) LDA eigenenergies for one snapshot $\{R(t)\}$ of a 2×2 5TBA monolayer supercell (each unit cell has two 5TBA oligomers; thus, there are 392 atoms in the supercell) with room-temperature random thermal atomic displacements. Table I compares the CPM with SCF LDA for the first few hole eigenenergies of the 2×2 system for several different snapshots. From both Fig. 1 and Table I, we see that the CPM eigenenergies are close to the SCF LDA eigenenergies. This establishes the CPM as a good method to describe the ground states of our system.

Using CPM, at any given time t , with $\{R(t)\}$ provided by the classical force-field MD simulation, we can construct the

TABLE I. The eigenenergies comparison between the SCF DFT and the CPM calculations for different atomic configurations of a 2×2 herringbone structure supercell.

	Method	VBM (eV)	VBM-1 (eV)	VBM-2 (eV)
$T = 0$ K	SCF DFT	0.095	-0.066	-0.148
Relaxed	CPM	0.092	-0.068	-0.150
$T = 300$ K	SCF DFT	0.153	0.008	-0.056
Snapshot 1	CPM	0.174	0.023	-0.008
$T = 300$ K	SCF DFT	0.143	0.008	-0.046
Snapshot 2	CPM	0.158	0.034	-0.047

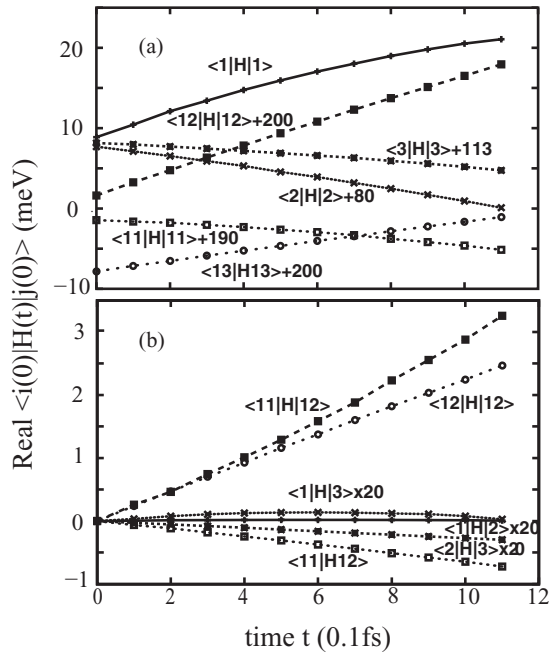


FIG. 2. The matrix elements of $H(t)$ under the basis set of $\{\varphi_i(t_1)\}$. Here the number in the Dirac bracket is the index “ i ” of the adiabatic state basis function. Here $i = 1$ means the VBM state, $i = 2$ means the VBM-1 state, and so on. This is true for all the figures. The +200, +113, +80, +190 in (a) are the amount of shifts in milli-electron volts in order to bring these curves together for viewing. This is for the 7×7 supercell system.

Hamiltonian $H(t)$ easily. Now the task is to integrate Eq. (5). To do that, a small time step of $dt = 10^{-3}$ fs is needed. This requires the evaluation of ε_i and V_{ik} at every 10^{-3} -fs interval. Calculating them directly by solving the Schrödinger Eq. (3) for every 10^{-3} fs is prohibitively expensive. Here, we will introduce a linear-time-dependence approximation for $H(t)$. According to this approximation, within a time interval $[t_1, t_2]$ (here $\Delta t = t_2 - t_1$ is of the order of femtoseconds), the Hamiltonian $H(t)$ will have the following linear dependence on time t :

$$H(t) = H(t_1) + (t - t_1)(H(t_2) - H(t_1))/(t_2 - t_1). \quad (7)$$

To test this approximation, we have represented $H(t)$ on the basis of the adiabatic eigenstates at t_1 : $\{\varphi_i(t_1)\}$. Some of the typical matrix elements, $\langle \varphi_i(t_1)|H(t)|\varphi_j(t_1)\rangle$, are shown in Fig. 2. As we can see, these matrix elements are approximately linear within a 0.5-fs time interval Δt . Now we first solve Eq. (3) for every Δt (0.5 fs). From that, we have $\{\varepsilon_i(t_1), \varphi_i(t_1)\}$ and $\{\varepsilon_i(t_2), \varphi_i(t_2)\}$. In our cases, we have solved 50 top VB states ($i = 1, 50$) near the band edge for the 7×7 supercell system. These $M = 50$ states span an eigenenergy window of about 0.35 eV, which is large enough since the average energy of $\psi(t)$ is only about 0.05 eV below the VBM energy, as will be shown later, and the coefficient $C_{50}(t)$ in Eq. (5) is already extremely small (on the order of 10^{-11} to 10^{-15}). Furthermore, when changing M from 50 to 40, we see no significant differences in our simulated results.

Now we will use $\{\varphi_i(t_1)\}_{i=1, M}$ as the basis set to diagonalize $H(t)$. To do that, we need the matrix elements $\langle \varphi_i(t_1)|H(t)|\varphi_j(t_1)\rangle$ for t within $[t_1, t_2]$. Obviously,

we have $\langle \varphi_i(t_1)|H(t_1)|\varphi_j(t_1)\rangle = \varepsilon_i(t_1)\delta_{i,j}$. Therefore, all we need is the matrix element $\langle \varphi_i(t_1)|H(t_2)|\varphi_j(t_1)\rangle$ in order to use Eq. (7) to obtain $\langle \varphi_i(t_1)|H(t)|\varphi_j(t_1)\rangle$. However, we know $\langle \varphi_i(t_2)|H(t_2)|\varphi_j(t_2)\rangle = \varepsilon_i(t_2)\delta_{i,j}$. Let us now assume $\{\varphi_i(t_1)\}$ can be expanded by $\{\varphi_i(t_2)\}$ as $\varphi_i(t_1) = \sum_{j=1, M} \langle \varphi_j(t_2)|\varphi_i(t_1)\rangle \varphi_j(t_2)$, then $\langle \varphi_i(t_1)|H(t_2)|\varphi_j(t_1)\rangle$ can be obtained from $\langle \varphi_i(t_2)|H(t_2)|\varphi_j(t_2)\rangle = \varepsilon_i(t_2)\delta_{i,j}$ by a simple unitary transformation. In reality, the transformation $\varphi_i(t_1) = \sum_{j=1, M} \langle \varphi_j(t_2)|\varphi_i(t_1)\rangle \varphi_j(t_2)$ is not unitary due to the lack of completeness of the basis set. We have carried out a Gram-Schmidt orthonormalization to make the matrix $\langle \varphi_j(t_2)|\varphi_i(t_1)\rangle$ unitary. Since most of this Gram-Schmidt modifications happen to the high eigenstates i (when i is close to M), and since the coefficients $C_i(t)$ of Eq. (4) of these high eigenstates i are very small, the overall error of this procedure on $\psi(t)$ is very small.

We can now summarize our procedure to integrate Eq. (5) as the following: At every time interval Δt ($=0.5$ fs), say t_1 and $t_2 = t_1 + \Delta t$, we solve Eq. (3) to obtain the corresponding $\{\varepsilon_i(t_1), \varphi_i(t_1)\}$ and $\{\varepsilon_i(t_2), \varphi_i(t_2)\}$. Then, we use a smaller time step dt ($=10^{-3}$ fs) to integrate Eq. (5) from t_1 to t_2 . In reality, dt can also be adjusted dynamically in order to integrate Eq. (5) accurately judged by some criterion, e.g., the conservation of the wave-function norm. Nevertheless, in all these procedures, dt is of the order of 10^{-3} fs. During this integration, at every dt step, we diagonalize an $M \times M$ ($M \sim 50$) matrix $\langle \varphi_i(t_1)|H(t)|\varphi_j(t_1)\rangle$ obtained using the linear-time-dependent approximation of Eq. (7) and the procedure described above. This will give us $\{\varepsilon_i(t), \varphi_i(t)\}$ at every dt interval, which can be used to evaluate $V_{ik}(t)$ from Eq. (6) and to integrate Eq. (5).

It is interesting to note that a similar linear approximation on H could be used for real-time integration of TDDFT.⁴⁷ There, time-dependent wave functions for all the occupied states must be calculated. One might be able to choose different set of $\{\varphi_i(t_1)\}$ for different electron orbitals; thus, M can remain small. Note also that the use of multiple and adjustable time steps to integrate the wave function in Eq. (5) has been done before,⁵⁰ although a constant V_{ik} had been used within the large time interval Δt . In our paper, $V_{ik}(t)$ is evaluated at every dt as described above, which makes a critical difference [since $V_{ik}(t)$ can change sharply within the timescale of 10^{-3} fs; as we will see later in Fig. 9, where the sharp peak in the transition rate R_i is related directly to the sharp peak in $|V_{ik}(t)|^2$]. Our use of linear time dependence of $H(t)$, instead of linear time dependences of $\varphi_i(t)$, $\varepsilon_i(t)$, or $V_{ik}(t)$, is in spirit similar to the idea of diabatic states,²⁹ because the $M \times M$ matrix elements of $H(t)$ within Δt are based on a fixed basis function set $\{\varphi_i(t_1)\}$ (hence the resulting matrix elements change slowly with time, although the matrix eigenvectors and eigenenergies $\varphi_i(t)$, $\varepsilon_i(t)$ can change rapidly near the anticrossing points). To further appreciate this point, one can look at a simple 2×2 time-dependent Hamiltonian: $H[1,1] = \alpha t$, $H[2,2] = -\alpha t$, $H[1,2] = H[2,1] = V$. If V is very small (a small anticrossing), then the eigenvectors and eigenenergies will change highly nonlinearly with time t , but the Hamiltonian matrix elements are clearly linear with t .

Based on the linear approximation of $H(t)$ in Eq. (7), we can use a time interval Δt of 0.5 fs to solve the Eq. (3), which is the most expensive step in the whole calculation. Thus, the new computational cost is similar to that of a conventional BO-MD.

This is the main contribution of the current work in terms of methodology developments. Furthermore, we have used the CPM to construct $H(t)$, thereby avoiding the need to do SCF DFT calculations. We can solve Eq. (3) using the folded spectrum method (FSM)⁵¹ based on the plane-wave basis set. However, we found it faster to use the overlapping fragment method (OFM)⁵² to diagonalize Eq. (3), especially when we need to solve $M = 50$ eigenstates. The OFM method has been used to solve the eigenstates of organic polymers and yielded good results compared with direct FSM calculations.⁵² In our OFM calculation, each five-ring 5TBA oligomer has been cut into three mutually overlapping fragments, each containing three thiophene rings with the cutoff bond passivated with additional H atoms. The eigenstates of each fragment are solved separately (with its charge density calculated by the CPM) using a small box with a plane-wave basis set. The VBM state of each fragment is used as the basis set to diagonalize the original full-system Hamiltonian $H(t)$. The detailed procedure of the OFM is described in Ref. 52. In Fig. 1, we show the OFM results for the 2×2 supercell system. We can see that, although there is a 150-meV shift to the ε_i curve, the overall shape of this curve agrees quite well with the original CPM + FSM result and the SCF DFT result. The constant overall shift will not affect the carrier dynamics that depends on the relative positions of the adiabatic states. Large errors only occur when the eigenenergy is 1.5 eV below the VBM, far from the energy range in which the ψ resides. We have also tested the 7×7 supercell system used for our final study. The OFM- and FSM-solved eigenstates look similar in their spatial localizations, and the eigenenergy changes between different atomic configurations are also similar for these two methods. For example, we have taken two snapshots in the MD trajectory, and the VBM eigenenergy difference between these two snapshots is -0.12 eV using FSM and -0.14 eV using OFM. This shows that OFM can quantitatively describe the eigenstates of the system and can be used for our NAMD-CPM simulations.

III. THE PHYSICAL SYSTEMS AND SIMULATION PROCEDURES

We have used the formalism described in Sec. II to calculate a 7×7 supercell of a 5TBA monolayer thin film. The system has 4802 atoms with 294 fragments in the OFM calculation. The structures of the thin film at room temperature and a single 5TBA oligomer are shown in Fig. 3. This is a system similar to a previous tetradecyl 5TBA (TD5TBA) monolayer⁵³ system studied by atomic force microscopy. The 5TBA monolayer has also been made experimentally, and its p -type carrier lateral mobility will be measured using microelectrodes.⁵⁴ Both the TD5TBA and 5TBA monolayers exhibit a herringbone packing pattern when viewed from the top as shown in Fig. 3. The 5TBA oligomer differs from the TD5TBA by not having the alkane chain on the top of the molecule. As a result, the 5TBA oligomers tend to stand up vertically within the monolayer, instead of leaning toward one side as in the TD5TBA case.⁵³

The system shown in Fig. 3 is simulated using consistent force field 91 (CFF91)⁵⁵ force fields. The force field calculated 5TBA lattice constants in the x and y directions (Fig. 3)

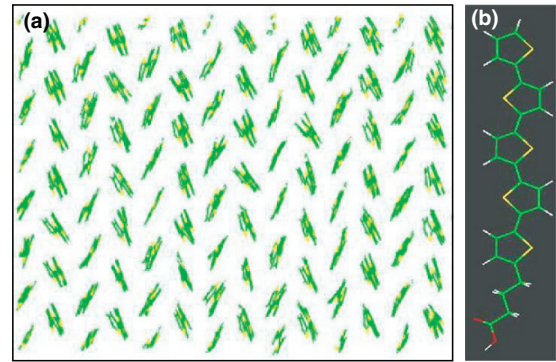


FIG. 3. (Color online) Top view of the herringbone pattern (a) of the 5TBA oligomer and (b) the side view of the 5TBA molecule. A 7×7 supercell with 4802 atoms is used in our study. In (b), the yellow indicates the S atom, green the C atom, white the H atom, and red the O atom. The classical force field is used in an MD simulation to provide the thermal fluctuation of the molecules at room temperature. The horizontal direction is defined as the x direction, while the vertical direction is defined as the y direction. The dimensions for these two directions for the 7×7 supercell are 53.20 and 39.90 Å, respectively.

are 7.6 and 5.7 Å, respectively, which agree well with the experiments.⁵⁴ The calculated standing-up molecule orientation in a herringbone pattern also agrees with the experimental observation.⁵⁴ Furthermore, a few bond-length parameters in the CFF91 are slightly modified, so the force field-relaxed single 5TBA molecule geometry agrees well with the LDA-relaxed geometry. A Verlet algorithm⁵⁶ is used to carry out MD using the code LAMMPS.⁵⁷ The MD simulation is done for several picoseconds where the average temperature equals 300 K. The last 1-ps trajectory is used in our NAMD-CPM calculation.

Using the $R(t)$ obtained from the classical MD, we then performed the NAMD-CPM calculation according to Eqs. (3)–(7) and the procedure described in Sec. II. The details of the parallel computation of $\{\varepsilon_i(t), \varphi_i(t)\}$ at every Δt are described in the Appendix C. Figure 4 shows the first few adiabatic eigenstate energies varying with time, and the isosurface plots of the corresponding eigenstates. In Fig. 4, we can see many state energy anticrossings, especially for the low-energy valence states. Sometimes one can trace one eigenstate, finding that its location does not change much although its energy can vary over 0.1 eV (e.g., the second VB state at $t = 0$, the pink state, which can be considered as the same state as the third VB state at $t = 12$ fs, the golden state).

After all the $\{\varphi_i(t), \varepsilon_i(t)\}$ are obtained, the $\psi(t)$ is integrated (following the procedure in Sec. II), starting with the adiabatic VBM state at $t = 0$. This integration part does not take much time.

The above steps finish the main task of integration of $\psi(t)$ following Eq. (1). In the following, we will discuss the simulation results based on the Ehrenfest dynamics (with its modification) and the FSSH dynamics; both are based on the solution of $\psi(t)$ but with different explanations and modifications in order to connect the results to carrier transport.

In the Ehrenfest dynamics, $|\psi(t)|^2$ describes directly the electron movement. The average energy of $\psi(t)$ is shown in Fig. 5(b) as the pink line. As we can see from Fig. 5(b),

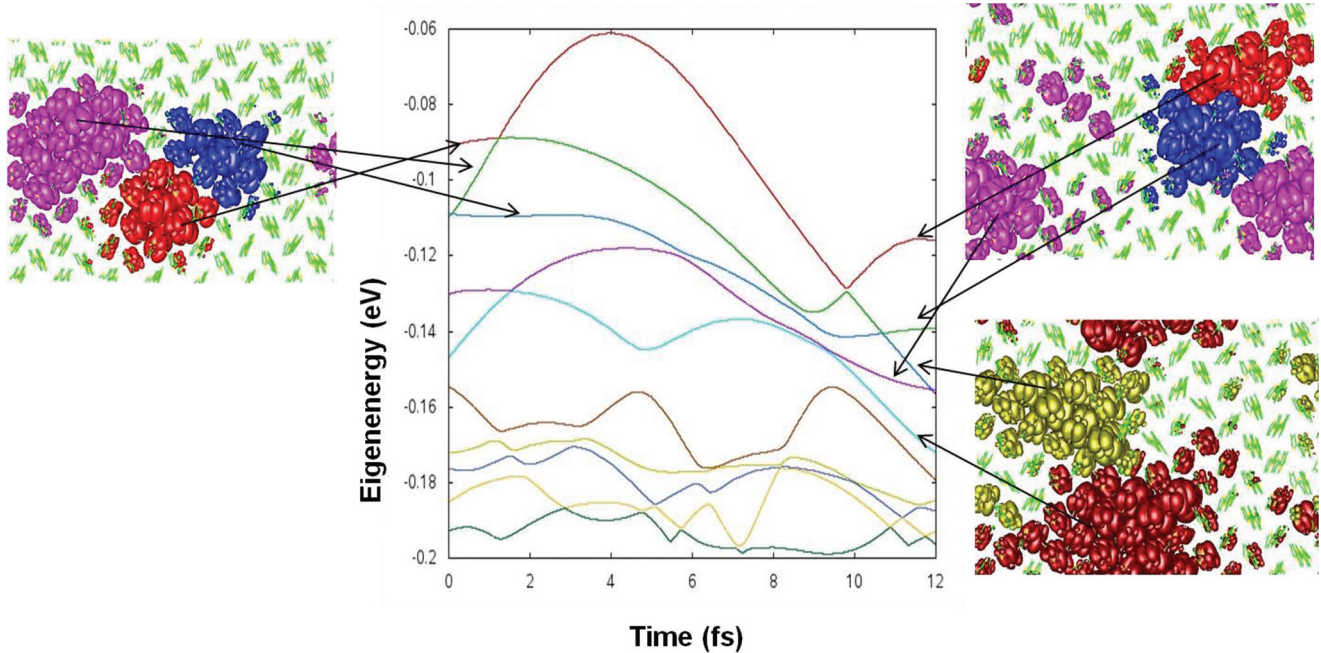


FIG. 4. (Color online) The adiabatic state eigenenergies (center) and the eigenstate isosurface plots (two sides). Each colored curve in the center panel represents one ε_i for one “ i .” The isosurface contains 98% of the charge density in $|\varphi_i(t)|^2$.

although at $t = 0$, the $\psi(0)$ equals $\varphi_1(0)$, the $\psi(t)$ quickly evolves into some kind of quasisteady state in a very short time (around 15 fs). Unfortunately, this quasisteady state is rather unphysical. It is about 0.2 eV below the VBM and seems to be in the middle of the 50 $\varphi_i(t)$ states chosen to be included in Eq. (4). This artifact is a consequence of the Ehrenfest dynamics⁵⁸ [Eqs. (1) and (2)]. In Ehrenfest dynamics, if the back reaction of the electron dynamics to nuclear dynamics is ignored, an infinite temperature distribution in the electron degree of freedom will result.⁵⁹ This is exactly what happened in our case. Furthermore, even if the full Ehrenfest dynamics with back reaction was used, a similar problem would exist as discussed in Refs. 39 and 59, and the effective temperature within the electronic degree of freedom, although not infinite, could be extremely high.⁵⁹ To further confirm this numerically, we have taken a simple one-dimensional model Hamiltonian from Ref. 44, which includes the coupling between the electron and nuclear dynamics. We have performed an Ehrenfest dynamics of this system that includes the back reaction. The result shows similar behavior as in Fig. 5(b).

Fundamentally, the above problem is a consequence of the classical treatment of nuclear movement using Newton’s law as discussed in Ref. 60. In a quantum-mechanical treatment of the nuclear movement, even at zero temperature (no atomic movement in the classical treatment), there is a zero-phonon mode, which can still induce transition from i to k as long as $\varepsilon_i < \varepsilon_k$ for the hole-state transition, but the transition from k to i cannot happen. This difference maintains the detailed balance between i and k and prevents the electronic system from overheating. All these are missing in the Ehrenfest dynamics.

Here, we provide an empirical approach to correct this detailed balance problem, especially under our detachment approximation. To introduce the effect of the quantum-mechanical zero-phonon mode, we will add a prefactor in

the time-dependent Schrödinger Eq. (5), and we have

$$\dot{C}_i(t) = -i\varepsilon_i(t)C_i(t) - \sum_k C_k(t)V_{ik}(t)f(\varepsilon_i - \varepsilon_k, t) \quad (8)$$

Here, if $R_{i,k} \equiv \text{Re}[C_k(t)C_i^*(t)V_{ik}(t)] > 0$ (the weight transition is from i to k), then $f(x, t) = 1$, if $x < 0$, and $f(x, t) = \exp(-x/kT)$, if $x > 0$. Similarly, if $R_{i,k} < 0$ (the weight transition is from k to i), then $f(x, t) = \exp(x/kT)$, if $x < 0$, and $f(x, t) = 1$, if $x > 0$. We will call the algorithm of Eq. (8) the ME algorithm. The result of this ME algorithm is shown in Figs. 5(a) and 5(b) as red lines. We can see that this time, the average energy of $\psi(t)$ is much closer to the VBM energy, and there is no overheating in the electronic degree of freedom. Some of the possible consequences of Eq. (8) are discussed in Appendix D.

Besides the Ehrenfest dynamics, another widely used MQC dynamics is Tully’s FSSH algorithm. While the original motivation of FSSH is to study chemical reactions and nuclear trajectory branching, here we use it to study the electron movement and carrier transport. In our case, the stochastic occupation of the energy surfaces in FSSH is not used to describe different nuclear trajectories, instead it is used to describe the electron movements. Within the detachment approximation (without the back reaction), there is no different nuclear trajectories (no branching) for different simulation runs (there is only one single nuclear trajectory). However, one can still have different occupations of the adiabatic states by the hole carrier (to simulate the hole transport) during different simulation runs. More specifically, if one runs many FSSH simulations, one can use a $P_i(t)$ to denote the hole’s probability of staying on the adiabatic state $\varphi_i(t)$ (the adiabatic energy surface) at time t . $P_i(t)$ does not equal $|C_i(t)|^2$ of Eq. (4). Instead, $\{P_i(t)\}$ is determined by a master equation with the transitions between different i s guided by the dynamics of

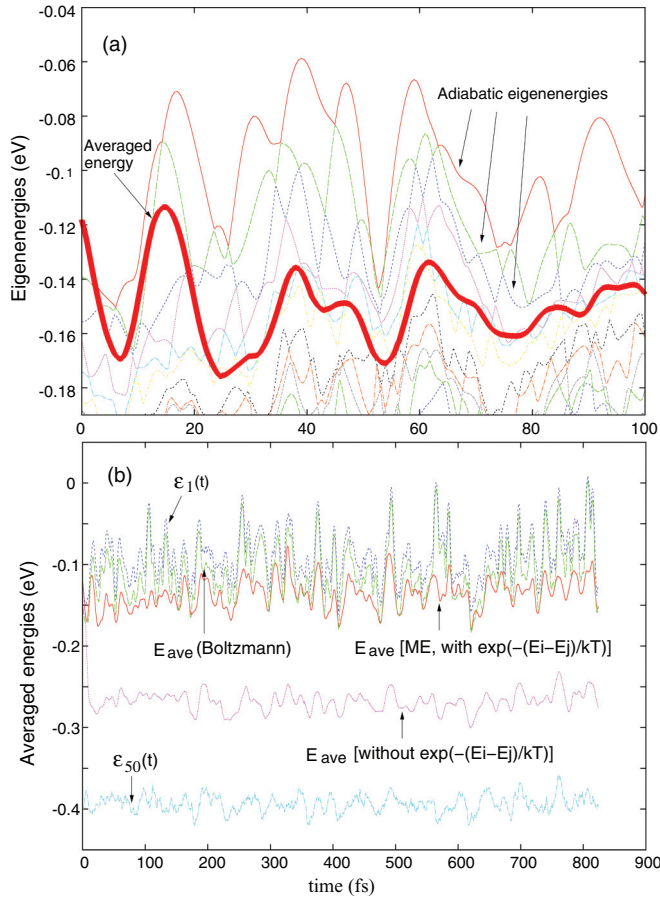


FIG. 5. (Color online) The adiabatic eigenenergies and the averaged $\psi(t)$ energy. (a) The enlarged view for only 100 fs. The thin lines are adiabatic eigenenergies, and the thick red line is the averaged $\psi(t)$ of the ME method using Eq. (8). (b) The full simulation plotting out only $\epsilon_1(t)$ and $\epsilon_{50}(t)$ (here i in ϵ_i is the index of the hole orbitals, starting from the top of VB state). The red line is the same as the thick red line in (a), while the pink line is original Ehrenfest dynamics without the Boltzmann factor in Eq. (8), and the green line is the average energy calculated using Boltzmann distribution from all the adiabatic eigenenergies $\{\epsilon_i(t)\}$.

$\psi(t)$ following the FSSH algorithm. Thus, $\psi(t)$ is used as an auxiliary variable, not as the real wave function to describe the electronic state. This technique was first used by Prezhdo *et al.*³⁶ to study carrier cooling in a quantum dot. One issue is how to maintain a detailed balance in FSSH under the detachment approximation without the back reaction. For that, we have followed the procedure used in Ref. 36. The details of our procedure are described in Appendix E.

Figure 6 shows the comparison between the ME and Tully's algorithm results. The plot shows that although the ME algorithm and Tully's algorithm give different average energies, they are close to each other and behave qualitatively in the same way.

At this point, it is useful to define a Boltzmann average energy. This is an average energy at time t according to the Boltzmann distribution among the adiabatic states φ_i : $\epsilon_{ave} = \sum_i \epsilon_i \exp(\epsilon_i/kT) / \sum_i \exp(\epsilon_i/kT)$. This energy is shown in Figs. 5(b) and 6. We can see that the Boltzmann average energy is higher than the two NAMD-CPM results and is much closer

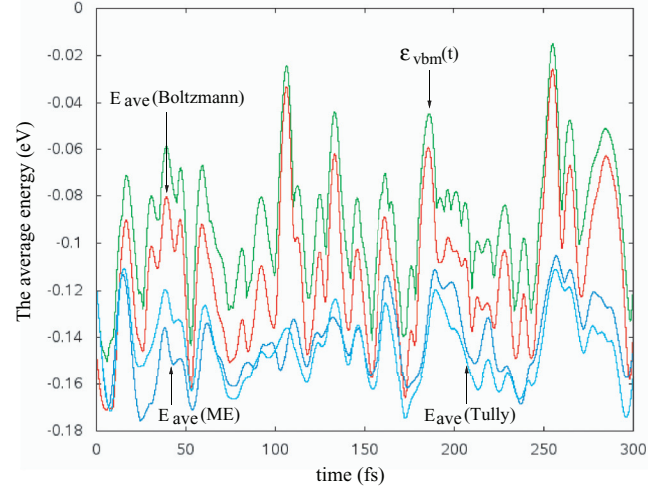


FIG. 6. (Color online) The comparison between the ME algorithm result and the Tully's algorithm result.

to the VBM. This is an important conclusion because in many phenomenological treatments, the Boltzmann distribution among adiabatic states is always assumed. Here, the reason that the NAMD-CPM results (either the ME algorithm or Tully's algorithm) fail to reach the Boltzmann distribution is the rapid eigenenergy fluctuations of the adiabatic states. The electronic system is not quick enough in responding to this fluctuation; thus, it is always lagging behind in a nonequilibrium state.

To further illustrate the difference between the ME and Tully's algorithms, in Fig. 7, we show the population $P_i(t)$ on the adiabatic state i in Tully's algorithm, and the $|C_i(t)|^2$ of

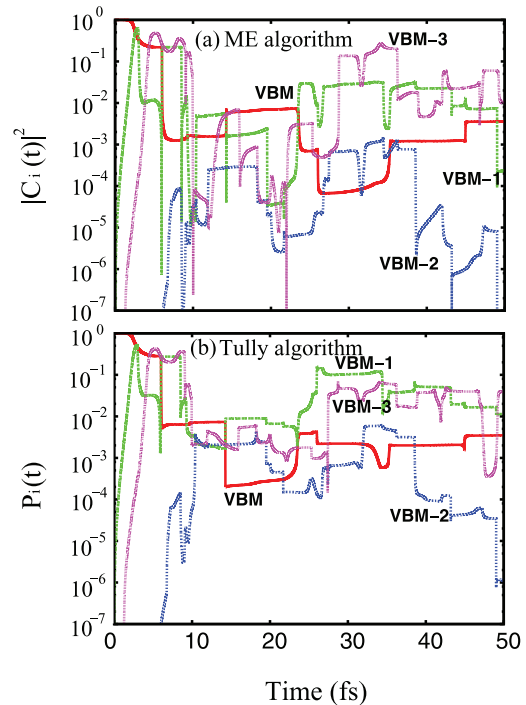


FIG. 7. (Color online) $|C_i(t)|^2$ in the ME algorithm (a), and $P_i(t)$ in Tully's algorithm (b). A sudden change in these quantities usually means a state crossing (as a result, the identity of the states exchanges).

Eq. (4) in the ME algorithm. We see that the $P_i(t)$ and $|C_i(t)|^2$ can change suddenly, but that is due to the state anticrossing, where the indexes of the two anticrossing states exchanged. At the beginning, when $|C_i(t)|^2$ and $P_i(t)$ started from the same occupation (e.g., VBM), the first few states in ME and Tully's algorithm look similar. But when their amplitudes become small, their behaviors are quite different. This means the $P_i(t)$ in Tully's algorithm and $|C_i(t)|^2$ in the ME algorithm can be very different when both of them are very small. Note, both $P_i(t)$ in Tully's algorithm and $|C_i(t)|^2$ in the ME algorithm are mainly distributed among four to seven states near the top of the VB.

IV. SIMULATION RESULTS AND CARRIER TRANSPORT MECHANISMS

The main scientific goal of the current study, besides the algorithm development, is to reveal the underlying mechanism of the carrier transport in the monolayer thin film of 5TBA. An organic molecule crystal can be classified into different categories according to its relative strengths between intermolecular coupling, molecule reorganization energy, and thermal fluctuation. Our case belongs to a relatively large thermal fluctuation and intermolecular coupling. Prior to the calculation, different mechanisms can be hypothesized for carrier transport: (1) band structure transport by extended bulk Bloch states;³ (2) polaron hopping, where polaron localization is induced by atomic relaxation caused by the hole state;⁶ (3) localized state drifting, where the localization is induced by molecule thermal fluctuation, and the same fluctuation can cause localized states to change their positions with time. Thus, carrier mobility is produced by the state drifting (while the hole is residing on the same state without any state transition); (4) localized state transitions by absorption/emission of a single phonon as described by a simple Fermi golden rule;⁵ (5) localized state energy anticrossing, where they cross each other in energy and the carrier residing on one state can jump to another state.

There are many band structure calculations for periodic organic structures.^{61–63} The underlying assumption is that band structure and effective mass can be relevant to carrier transport through a bulk transport picture. Our calculation shows that at room temperature, the adiabatic states are localized among 10–20 5TBA oligomers, as shown in Fig. 4. Thus, the wave function is not extended, and hypothesis (1) is invalid.

Another common picture is that the wave function will localize in a single unit (e.g., a molecule, or the oligomer, in our case) of the structure and form a polaron.⁶⁴ Then, it will hop from one unit to another. In such a polaron picture, localization is induced by atomic relaxation due to strong electron-phonon coupling (not by thermal fluctuation); thus, it will happen at zero temperature. To investigate the possible formation of a polaron, we have performed DFT/LDA calculations with a 2×2 supercell (which contains eight 5TBA oligomers) with one hole at zero temperature. In our calculation, we intentionally introduced an initial distortion to the atomic positions and an initial hole wave-function localization. But after SCF iterations and atomic relaxation, the hole wave function becomes extended uniformly in the 2×2 supercell, and there is no localization. This means that, according to LDA,

at zero temperature there is no polaron, or at least no polaron with wave-function localization smaller than eight 5TBA oligomers (or smaller than the thermal fluctuation-induced localization as shown in Fig. 4). We do caution that, due to the self-interaction error,⁶⁵ LDA has a tendency to delocalize the wave function, making the formation of polaron more difficult. Future investigation using more accurate methods might be necessary, although a preliminary study with an algorithm that removes the self-interaction energy within LDA has also failed to find localized polaron state.⁶⁶ This conclusion is consistent with our recent study for naphthalene⁶⁷ and the work by Troisi⁶⁸ for pentacene and rubrene organic crystals. Under this circumstance, in order to further estimate the importance of the polaronic effects, we have checked the reorganization energy that can be estimated reliably by LDA calculations.⁶⁹

Our LDA calculated single 5TBA molecule reorganization energy (defined as the energy drop due to atomic relaxation after a hole is placed in the original neutral system) is 99 meV, which is similar to the single molecule neutral to the charge state atomic relaxation energies of pentacene (55 meV)⁷⁰ and rubrene (79 meV).⁶⁹ Both neutral and charged (with one-hole) 5TBA molecules have a planar relaxed geometry. Thus, the torsion angle rotation does not contribute significantly to this reorganization energy. From the 2×2 supercell system DFT calculation, we have a corresponding LDA reorganization energy of 20 meV for that system due to a larger hole localization volume. Since the thermal fluctuation-induced wave function localizations shown in Fig. 4 are similar to the 2×2 supercell size, we expect that the atomic relaxation energies of these localized states should be also around 20 meV. This energy is much smaller than the ~ 100 - to 200 -meV energy fluctuations of VBM shown in Figs. 5 and 6, which is induced by thermal fluctuation. Thus, the polaronic effect is much smaller than the thermal fluctuation effect.

A third way to estimate the magnitude of the polaronic effect is to calculate the atomic force changes when the system is occupied with one hole. To do this, we have taken a snapshot of the 2×2 supercell during a room-temperature MD. The LDA atomic forces of the N -electron neutral system and the $N-1$ electron system are calculated. The atomic force difference between these two systems is about 1.6% of the average atomic forces (thermal fluctuation forces) in the system. This means the polaronic effect is small in its impact on nuclear trajectory.

The above investigation of the polaronic effect can be summarized as the following: (a) There is no polaron formation at zero temperature, and any polaronic effect is smaller than the thermal fluctuation (dynamic disorder) effect; (b) Since the polaronic effect is not included in our detachment approximation (no electron to nuclear back reaction), the item (a) also justifies the use of the detachment approximation in our simulation. Item (a) means the hypothesis (2) does not hold, and the main reason for localization is the thermal fluctuation (dynamic disorder), not the reorganization-induced self-trapping polaron.⁷¹

We now discuss the points (3), (4), and (5). Figure 8 shows the diffusion distance square as a function of time t . Note that this is done for $\psi(t=0) = \varphi_{\text{VBM}}(t=0)$. However, recalculating this diffusion distance starting from a steady state (e.g., after 10 fs) does not significantly change the result. The 7×7

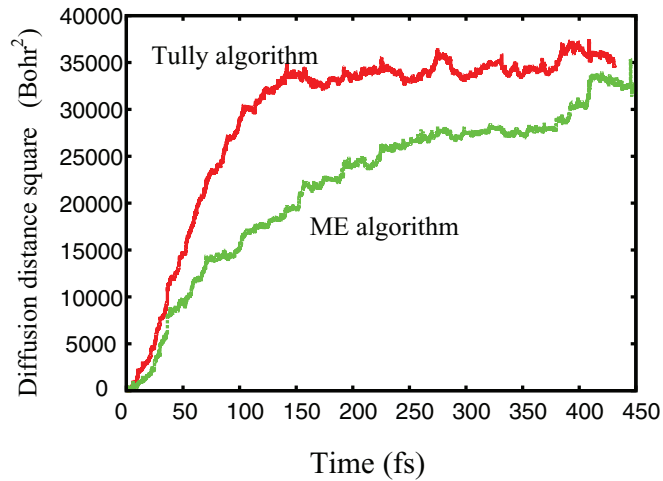


FIG. 8. (Color online) The diffusion distance square as a function of the simulated time t .

supercell is still relatively small. To calculate the diffusion distance, we have repeated the system a few times in its x and y directions and treat the image states of an adiabatic state $\varphi_i(t)$ as different states (e.g., with a different coefficient $C_i[t]$ in Eqs. (4) and (7) and different $P_i[t]$ in Tully's algorithm). This allows us to have a larger diffusion distance than the box size of the 7×7 supercell. Nevertheless, this technique has its limitations, and as a result, the diffusion distance is saturated eventually both for the ME algorithm and Tully's algorithm. Thus, we should only judge carrier mobility from the time region before the saturation. We have also simulated a 10×10 supercell system with a shorter time span (60 fs) following the exact same procedure. The 10×10 supercell simulation yields a similar result compared with the 7×7 supercell result for the diffusion distance square as a function of time.

From Fig. 8, we see that initially the ME and Tully's algorithms have similar results. However, after some time (50 fs), Tully's algorithm yields a bigger diffusion distance. It is interesting to speculate whether the slowdown in the ME algorithm is related to the weak localization phenomenon in a disordered system, where coherently constructive backscattering can slow carrier diffusion.⁷² Further study is needed in the future to resolve this point. From the slope of the line in Fig. 8 (taken from the Tully's algorithm result), if we use a two-dimensional (2D) diffusion formula of $d^2 = 4Dt$ and $\mu = eD/kT$, we obtain a hole mobility μ as $44 \text{ cm}^2/\text{Vs}$. This is a bit large, considering that most organic crystals have mobilities between 1 and $10 \text{ cm}^2/\text{Vs}$. Although we are still waiting for experimental measurement of the mobility for our system,⁵⁴ recently a thin film of 2,7-dioctyl[1]benzothieno[3,2-b][1]benzothiophene was synthesized with a similar structure as in Fig. 3. The maximum mobility reported⁷³ is $31 \text{ cm}^2/\text{Vs}$, which is close to our result.

To determine whether the diffusion is caused by state position drifting, we have plotted the center-of-mass position of the first adiabatic state (VBM) in Fig. 9 as a function of time. We see that when there is no state anticrossing, the position of the state does not change, despite that the energy of the state can change by as much as 0.1 eV during the same period. The same is confirmed by looking at the states in Fig. 4 (e.g.,

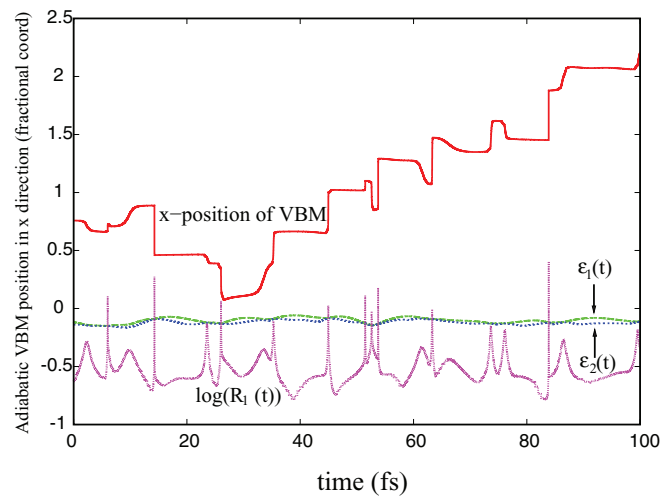


FIG. 9. (Color online) The center of mass position of the VBM state. Also shown are the eigenenergies of the first two adiabatic states, and the total transition rate $R_1(t)$ (defined as $R_i \equiv \sum_k |R_{i,k}|/|C_i|^2$) from the VBM state. A peak in the transition rate $R_1(t)$ indicates a state crossing between the VBM and VBM-1 states. Also, at such crossing, the VBM state position suddenly changes, which is due to the change of identity between the VBM and VBM-1 state (the highest adiabatic state is called VBM), rather than a genuine shift of the state position.

the second state at $t = 0$, and the third state at $t = 12$ fs in Fig. 4). In Fig. 9, when the VBM and VBM-1 states cross, the identities of the states switch, which can cause a sudden change of the VBM position in the plot. Nevertheless, from the flat plateau in the state position between the state crossings, we can conclude that the state position drifting proposed in hypothesis (3) should be small.

Next, we have investigated the state transition by absorbing or emitting a single phonon. Such a transition is used to explain carrier mobility in a disordered polymer system.⁵ But here, the adiabatic state localizations are caused by thermal fluctuations, not by the disorder tangling/arrangement of polymer chains. Thus, the state here can change more rapidly than in the disordered polymer system. In Tully's algorithm (similar procedure can be used for the ME algorithm), we can turn off any energy surface hopping between states i and k when $|\varepsilon_i - \varepsilon_k| > 5 \text{ meV}$. Since most phonon modes have a phonon energy larger than 5 meV, this will effectively turn off all the single-phonon absorption/emission effects. The resulting diffusion distance square is very similar to the original one as shown in Fig. 10. This means the effect of single-phonon absorption/emission transition as described in hypothesis (4) is rather small and can be ignored. We can thus conclude that all transitions happen when two states anticross each other in their energies. When that happens, a fast transition of the wave function weight from one state to another state takes place. That causes the position of the carrier to suddenly jump, and this jump [as described in the hypothesis (5)] is the real cause for carrier mobility in our system.

There are interesting differences and similarities between the state anticrossing observed in our simulation and the state anticrossing in the Marcus theory.⁷⁴ In both cases, the state anticrossing plays an important role, and the transition

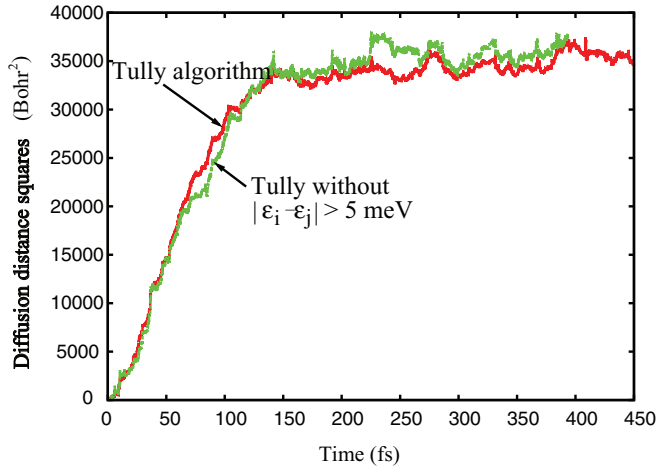


FIG. 10. (Color online) The diffusion distance squares with and without the $|\varepsilon_i - \varepsilon_j| > 5$ -meV transitions.

happens during the state anticrossing. In the Marcus theory, the localization is either formed by a geometric confinement (e.g., within a molecule or inside a quantum dot) or is due to reorganization (e.g., in a polaron). The reorganization energy can also be used as a measure for the energy barrier that needs to be overcome to have the state anticrossing. On the other hand, in our current problem, the localization of the state and the state energy fluctuation are both caused by dynamic disorder induced by thermal fluctuation (not by reorganization energy). That we have such state anticrossing, while ignoring the hole-induced atomic relaxation, indicates fundamental differences between these two pictures. We thus expect very different temperature dependences on the mobility (because in our case, state localization, not just state energy fluctuation, also depends on the temperature).

It is also interesting to note the relationship between our picture and the dynamic disorder picture proposed by Troisi and Orlandi.⁴⁴ In their simulations, a model Hamiltonian is used, which includes the fluctuation of the intermolecular coupling. They have used pure Ehrenfest dynamics to monitor the diffusion of the electron wave function. In both their picture and ours, carrier mobility is driven by this thermal fluctuation (dynamic disorder). However, our simulation included the surface hopping in Tully's algorithm or the additional Boltzmann factor in the ME. Thus our procedures depend on the analysis of the wave function $\psi(t)$ in terms of adiabatic states $\{\varphi_i(t)\}$. As a result, we introduced the concept of state anticrossing and point out that this is the main underlying mechanism of the diffusion. Such analysis is absent from a pure Ehrenfest dynamics description. We have also used a parameter-free *ab initio* realistic DFT Hamiltonian, which includes both intra- and intermolecular fluctuations. The intramolecular fluctuation is important because it can contribute significantly to the localized state energy fluctuation, which causes the state anticrossing. In a way, this is also like the Marcus theory where the internal phonon degree of freedom causes the energy fluctuation to overcome the potential barrier. However, it will be interesting in the future to study the contributions of different phonon modes, especially the quantum-mechanical effects on these phonon modes that are not included in our classical MD simulations.

Finally, it should be noted that the carrier-diffusion mechanism we found can perhaps be described under a general Haken-Strobl-Reineker (HSR) framework.^{75,76} In the HSR model, a time-dependent random fluctuation term is introduced in the electron Hamiltonian to describe either on-site energy fluctuations or off-site interaction fluctuations. However, the analytical solution of such models is often found without using the picture of state localizations and the transition from one localized state to another.^{77,78}

V. CONCLUSION

We have presented several techniques to carry out a large-scale simulation for NAMD-CPM. These techniques and supercomputer facilities allow us to do NAMD-CPM for a 1 ps evolution of a 4802-atom system in a few hours. More specifically, (1) a linear time-dependent Hamiltonian within an interval Δt is introduced, which increases the simulation time step (of the computationally most expensive part) from $dt = 10^{-3}$ fs to $\Delta t = 0.5$ fs, thus reducing the overall computational cost by hundreds of times; (2) the ME dynamics procedure is proposed, which restores the detailed balance within the framework of Ehrenfest dynamics. It can be used as an alternative approach to Tully's algorithm to study carrier transport. (3) The nuclear movement and electronic movement are detached, and a classical force field is used for the nuclear movement. Detailed analysis is presented to justify this detachment treatment for the system studied. (4) The CPM is used to construct the Hamiltonian, while the OFM is used to diagonalize the Hamiltonian matrix. (5) The whole approach can be carried out using massively parallel computers and can be scaled to 50 000 cores. As a result, the whole calculation takes only a few hours.

We have used this approach to study the carrier transport of a 5TBA monolayer thin film. Such thin film has been synthesized experimentally. Our main task is to reveal the underlying mechanism of hole transport in such a system. This system demonstrates a herringbone 2D crystal structure and thus can be used as one prototype for other 2D organic molecular crystals. Through our calculation, we found that carrier transport is mostly induced by state anticrossing between localized states. The localizations of the states are caused by the dynamic disorder induced by thermal fluctuation, rather than by polaronic atomic relaxation. Thus, the state anticrossing mechanism is very different from the ones described by the Marcus theory. The state localization size is about 10–20 5TBA oligomers. In our simulation, we also found that the occupations of the adiabatic states are often in a nonequilibrium situation. The average energy calculated by the Boltzmann distribution among the adiabatic states is much closer to the VBM energy than the NAMD-CPM-simulated results.

ACKNOWLEDGMENTS

We thank F. Martin, B. L. M. Hendriksen, and M. Salmeron for stimulating discussions. J. F. Ren and L.-W. Wang were supported by the Office of Science (SC), Basic Energy Sciences, and Materials Sciences Engineering Division of the US Department of Energy under Contract No. DE-AC02-05CH11231. This research used resources of the Oak Ridge Leadership Computing Facility, located

in the National Center for Computational Sciences (NCCS) at Oak Ridge National Laboratory, which is supported by the SC of the Department of Energy under Contract No. DE-AC05-00OR22725. The computer time was allocated by the Department of Energy's Innovative and Novel Computational Impact on Theory and Experiment program. N. Vukmirović was supported by European Community FP7 Marie Curie Career Integration Grant (ELECTROMAT), Serbian Ministry of Science (ON171017), and FP7 Projects PRACE-2IP, PRACE-3IP, HP-SEE, and EGI-InSPIRE.

APPENDIX A: NEGLECTING THE ELECTRON TO NUCLEI BACK REACTION

In many cases, the very reason to do nonadiabatic MD is to study the back reaction (e.g., in collision and catalysis). To study carrier dynamics, we focus more on the behavior of the electronic system, not the nuclear system. The detachment approximation (neglecting the back reaction) has been used to study carrier cooling in a quantum dot,³⁶ line shapes in spectroscopy,⁷⁹ and exciton dynamics.⁸⁰ For a carrier dynamics study, the main approximation of the detachment approach is the neglecting of the polaronic effect that can change the carrier dynamics. In this effect, the occupation of a localized hole state induces atomic relaxations (reorganization), which further localizes the hole wave function. In Sec. IV of the main text, we show that the polaronic effect in our system is rather small, and the wave-function localization is induced mostly by dynamic disorder, rather than polaronic reorganization effect. The reorganization energy in the current system is less than 20 meV, while the dynamic disorder-induced adiabatic eigenenergy fluctuation is in the range of 100 to 200 meV. Recently, Wang *et al.*⁸¹ also studied the consequences of ignoring the back reaction to carrier mobility using a model Hamiltonian with Ehrenfest dynamics. They found that back reaction can reduce carrier mobility (as it induces wave-function localization). But if the diffusion is fast enough (e.g., carrier mobility is larger than 0.14 cm²/Vs in a 2D system), the back reaction can be safely ignored. As we show later, our calculated carrier mobility is about 44 cm²/Vs for our effective 2D system. This confirms that it is safe to ignore the back reaction in our problem. Another way to test the amplitude of the back reaction is to calculate directly the change of atomic force due to the occupation of a localized hole state. As discussed in Sec. IV, when one of the thermal fluctuation-induced localized states (see Fig. 4) is occupied by a hole, the change of atomic forces is only about 1.6% of the thermodynamically induced atomic forces. This means the back reaction will not significantly alter the nuclear trajectory. All these points support the use of the detachment approximation for our system. In this detachment treatment, the nuclear subsystem conserves its own total energy; thus, it has a microcanonical dynamics, while the electronic subsystem is in a canonical dynamics with a fixed temperature.

APPENDIX B: THE USE OF A CLOSED-SHELL SYSTEM FOR SCHRÖDINGER EQUATION

One important issue is what charge density to be used to construct $H(t)$ of Eq. (1), whether it should be the charge

density $\rho_0(r)$ of the N -electron closed-shell system or the charge density $\rho(r) = \rho_0(r) - \psi^2(r)$ of the actual $N-1$ electron system we are simulating. If the Kohn-Sham equation of the LDA Hamiltonian is to be used directly, then the $\rho(r)$ of the $N-1$ electron system should be used. However, this will introduce an erroneous Coulomb self-interaction of the single-particle state ψ .⁶⁵ As it turns out, it will be more accurate to use $\rho_0(r)$ instead of $\rho(r)$ to construct the $H(t)$ in Eq. (1). To understand this, we can investigate the N th eigenenergy ε_N of $H(t)$ and see which Hamiltonian will give more accurate result. We will denote the Hamiltonian of the N -electron system and $N-1$ electron system as $H(N)$ and $H(N-1)$, respectively. First, for an exact theory, the N th eigenenergy ε_N of $H(N)$ [$\varepsilon_N(N)$] and $H(N-1)$ [$\varepsilon_N(N-1)$] should be the same. The reason is the following: First, $\varepsilon_N(N) = \partial E(n)/\partial n|_{n \rightarrow N^-}$ and $\varepsilon_N(N-1) = \partial E(n)/\partial n|_{n \rightarrow N-1^+}$ (e.g., Janak's theorem for LDA calculation,⁸² Koopman's theorem for Hartree-Fock calculation,⁸³ or the corresponding theorem for random-phase approximation and GW calculation⁸⁴), here $E(n)$ is the total energy of the system with n electron (which could be fractional). Furthermore, under an exact theory, $E(n)$ should be a straight line between the interval $[N-1, N]$,^{85,86} which implies $\varepsilon_N(N) = \varepsilon_N(N-1)$. This is true under Koopman's theorem⁸³ for Hartree-Fock with frozen orbitals. Note that in Hartree-Fock, there is no self-interaction error. This has been shown to be approximately true for GW⁸⁷ Hamiltonian.⁸⁸ One can imagine using GW Hamiltonian to solve Eq. (1) and then using either $H_{\text{GW}}(N)$ or $H_{\text{GW}}(N-1)$ would be fine. Which LDA Hamiltonian, $H_{\text{LDA}}(N)$ or $H_{\text{LDA}}(N-1)$ is closer to $H_{\text{GW}}(N)$ or $H_{\text{GW}}(N-1)$? It has been shown that, for a closed-shell system (N -electron system), the nonlocal self-energy term $\Sigma(r, r')$ in $H_{\text{GW}}(N)$ is short ranged,⁸⁹ which can be approximated by the local exchange-correlation potential in $H_{\text{LDA}}(N)$.⁹⁰ While for the open-shell system ($N-1$ electron system), the self-energy term $\Sigma(r, r')$ in $H_{\text{GW}}(N-1)$ is long ranged, which cannot be approximated by the local exchange-correlation potential in $H_{\text{LDA}}(N-1)$. As a result, it will be better to use $H_{\text{LDA}}(N)$ to simulate the system. Recently, we have also used $H_{\text{LDA}}(N)$ (instead of $H_{\text{LDA}}(N-1)$) to calculate the shallow impurity levels with very accurate results.⁹¹ Thus, in conclusion, we should use $\rho_0(r)$ instead of $\rho(r)$ to construct $H(t)$ in Eq. (1).

APPENDIX C: DETAILS OF THE PARALLEL COMPUTATIONS

The adiabatic eigenstates and eigenenergies $\{\varphi_i(t), \varepsilon_i(t)\}$ are calculated for 825 fs. The calculation is executed on the Jaguarpf machine at the NCCS at Oak Ridge National Laboratory. The main task is to calculate $\{\varphi_i(t), \varepsilon_i(t)\}$ from Eq. (3) with an interval of 0.5 fs (thus, there are 1651 snapshots for the 825-fs simulation). In our case, we have the benefit that all the $\{R(t)\}$ are known before the calculation of $\{\varphi_i(t), \varepsilon_i(t)\}$ for this 825 fs. Thus, the calculations of Eq. (3) for different snapshots can be carried out in parallel. Typically, we calculate 22 snapshots simultaneously using 22 processor groups (snapshot group). We use 2352 computer cores for each snapshot group. Thus, in total, we have used 51 744 computer cores. In the OFM calculation, the 2352 cores in each snapshot group are further divided into 294 subgroups, each subgroup with eight cores. In this way, one

computer core subgroup (with eight cores) will calculate one fragment in OFM. Each snapshot group will typically have 25 snapshots (due to memory limitation) consecutively in time. In this way, one snapshot's calculation can start with the fragment wave functions of the previous snapshot, thus saving time for iteration convergence. One such calculation takes about 1 h of wall clock time, and we can obtain $22 \times 25 = 550$ snapshots (275 fs). Thus, the total calculation takes about 3 h. A plane-wave kinetic energy cutoff of 50 Ry is used in the calculation, norm-conserving nonlocal pseudopotentials⁹² are deployed, and the x , y , and z real-space grid points of the 7×7 supercell are 336, 252, and 224, respectively.

APPENDIX D: DISCUSSION OF THE ME DYNAMICS

The consequence of Eq. (8) is discussed further here. One might worry that the possible sudden change of $f(x, t)$ with time might interrupt the coherence of the wave-function evolution. The coherence wave-function evolution (e.g., the coherent accumulation of the wave-function weight from one adiabatic state to another adiabatic state) is important, for example, to describe a single-phonon absorption/emission event. More careful analysis, however, shows that such worries are unwarranted. For example, in a state energy anticrossing case, where the weight transition from one state to another can be large and rapid, the $|\varepsilon_i - \varepsilon_k|$ usually is very small, thus the effects of the factor $f(x, t)$ are small. In the case of a single-phonon absorption (or emission), the sign of $\text{Re}[C_k(t)C_i^*(t)V_{ik}(t)]$ does not change in the whole transition period (during which the coherent weight accumulation happens), thus the $f(x, t)$ does not change either during this period. Note that, in our approach, the time-dependent Schrödinger equation has been altered. But this is not the first scheme in which the Schrödinger equation has been changed in order to mimic the effect of dephasing or quantum-mechanical nuclear treatments. More abrupt interruptions happen in the wave-function collapsing scheme, where the ψ can instantaneously become one of φ_i .²⁴ Note that the total weight of wave function $\psi(t)$ is conserved throughout the time integration using Eq. (8). We are executing the ME dynamics under the detachment approximation. Thus, the nuclear subsystem conserves its own total energy in a microcanonical dynamics, while the electronic system is in a canonical dynamics with a fixed temperature T .

APPENDIX E: THE FSSH ALGORITHM UNDER THE DETACHMENT APPROXIMATION

One issue appears when deploying the FSSH algorithm under the detachment approximation, which is how to deal with the detailed balance during the hopping event. In FSSH, although $\psi(t)$ is calculated following Eq. (1), it is treated as an auxiliary variable, and the actual electronic system is represented by residing on one adiabatic state $\varphi_i(t)$ (i.e., on one adiabatic energy surface) at any given time t and its trajectory keeps hopping (switching) among different i s. Thus, the electronic property of the system at time t should be calculated based on $\varphi_i(t)$ (although the index i could suddenly change with time after the hopping), not on $\psi(t)$. The surface hopping from i to k is sudden (instantaneous), but the $\psi(t)$

will not change after the hopping; only the nuclear movement will be rescaled. The $\psi(t)$ is used to help determine how the system hops from one adiabatic state i to another state k . Note that this is a very different picture than the Ehrenfest dynamic, where the real electronic system is described by $\psi(t)$ and the electronic properties should be calculated based on $\psi(t)$.

In Tully's algorithm, when a state hopping from i to k is proposed, a related coupling degree of freedom in the nuclear system is calculated, and then the kinetic energy on this degree of freedom is checked. For a hole hopping, as in our case, if $\varepsilon_i < \varepsilon_k$, the hopping will always be allowed, and the velocity on the coupling degree of freedom will be rescaled, so its kinetic energy will be increased by $\varepsilon_k - \varepsilon_i$ after the hopping. If $\varepsilon_i > \varepsilon_k$, and the related kinetic energy is smaller than $\varepsilon_i - \varepsilon_k$, the hopping will be forbidden (it will not happen). If the kinetic energy is larger than $\varepsilon_i - \varepsilon_k$, the hopping will happen, but the velocity will be rescaled so its kinetic energy will be reduced by $\varepsilon_i - \varepsilon_k$. This procedure ensures that the total energy is conserved during the transition, and it treats the transition from i to k differently from the transition from k to i . This different treatment restores the detailed balance.⁹²

In our detachment treatment, the nuclear movement will not be affected by the hopping events in the electronic system. Thus, no rescaling of the nuclear kinetic energy will be performed, and no change of nuclear trajectory will happen. We have only one nuclear trajectory independently described by the classical force field. Nevertheless, if we have many stochastic runs, even though they will all have the same nuclear trajectory, we can still imagine the system having different electronic "trajectories" by residing on different adiabatic states following the FSSH algorithm. Over many runs, the probability of residing on adiabatic state φ_i at time t can be described by a weight (probability) function $P_i(t)$. Then the FSSH algorithm can be used to determine how the $P_i(t)$ changes with time [the master equation of $P_i(t)$]. The kinetic energy in the nuclear movement could still be used to determine whether an electronic hopping will be allowed (although rescaling after the hopping will not be performed). However, here we will introduce a further simplification. Instead of checking on the kinetic energy of the coupling degree of freedom explicitly on our nuclear trajectory for each proposed hopping, we will use a statistical approximation to represent this effect. In a statistical sense, the kinetic energy on the coupling degree of freedom follows the Boltzmann distribution. Thus, if we follow the FSSH procedure, and assuming a Boltzmann distribution to the relevant coupling nuclear kinetic energy, statistically it is equivalent to say that when $\varepsilon_i < \varepsilon_k$, the transition is always allowed, and when $\varepsilon_i > \varepsilon_k$, the transition will happen with a probability of $\exp(-(\varepsilon_i - \varepsilon_k)/kT)$ (due to kinetic-energy forbiddance). Then, in the master equation governing the evolution of $P_i(t)$, we have the following transition rates from $P_i(t)$ to $P_k(t)$ as described by FSSH formula: $R'_{i,k}(t) = \text{fac} \times \text{Re}[C_k(t)C_i^*(t)V_{ik}(t)]/|C_i(t)|^2$ with an additional prefactor $\text{fac} = 1$ for $\varepsilon_i < \varepsilon_k$ and $\text{fac} = \exp(-(\varepsilon_i - \varepsilon_k)/kT)$ for $\varepsilon_i > \varepsilon_k$.

Here, we can also estimate the effect of the rescaling in the kinetic energy during a hopping event in the original FSSH algorithm, which is ignored in our detachment approximation. Such rescaling can be important for small molecular systems

where the additional kinetic energy goes to one or two degree of freedoms and when the transition energy is large. In our problem, the localized wave function occupies a space of roughly 400 atoms. Thus, the transition degree of freedom might well consist of a few hundred atoms. After the kinetic-energy scaling, each atom might have roughly $\sim |\varepsilon_i - \varepsilon_k|/100$ additional kinetic energy (we use 100 atoms in a conservative estimation). In our case, the $|\varepsilon_i - \varepsilon_k|$ is very small. Actually, as discussed in Sec. IV, and Fig. 10, $|\varepsilon_i - \varepsilon_k|$ is likely to be less

than 5 meV. Then, in average, in the transition area, each atom will gain 0.05 meV, which is much smaller than its thermal kinetic energy of $3^*kT = 75$ meV. If we take the 100 atom as a whole, the gaining (or losing) of the 5 meV for this assembly is also much smaller than the stochastic fluctuation of its total kinetic energy, which equals: $kT\sqrt{3} \times 100 = 433$ meV. Thus, the possible local heating (or cooling) effect on the nuclear subsystem due to the hopping event is extremely small and hence can be ignored.

*lwwang@lbl.gov

¹V. Coropceanu, J. Cornil, D. A. da Silva Filho, Y. Olivier, R. Silbey, and J.-L. Bredas, *Chem. Rev.* **107**, 926 (2007).

²N. Karl, *Synth. Met.* **133-134**, 649 (2003).

³L. Giuggioli, J. D. Andersen, and V. M. Kenkre, *Phys. Rev. B* **67**, 045110 (2003).

⁴Y. C. Cheng, R. J. Silbey, D. A. da Silva Filho, J. P. Calbert, J. Cornil, and J.-L. Bredas, *J. Chem. Phys.* **118**, 3764 (2003).

⁵N. Vukmirovic and L. W. Wang, *Nano Lett.* **9**, 3996 (2009).

⁶A. N. Sokolov, S. Atahan-Evrenk, R. Mondal, H. B. Akkerman, R. Sanchez-Carrera, S. Granados-Focil, J. Schrier, S. C. B. Mannsfeld, A. P. Zoombelt, Z. Bao, and A. Aspuru-Guzik, *Nat. Commun.* **2**, 437 (2011).

⁷Z. Shuai, L. Wang, and Q. Li, *Adv. Mater.* **23**, 1145 (2011).

⁸K. Hannewald, V. M. Stojanovic, J. M. T. Schellekens, P. A. Bobbert, G. Kresse, and J. Hafner, *Phys. Rev. B* **69**, 075211 (2004).

⁹A. Troisi, *J. Chem. Phys.* **134**, 034702 (2011).

¹⁰J.-D. Picon, M. N. Bussac, and L. Zuppiroli, *Phys. Rev. B* **75**, 235106 (2007).

¹¹G. S. Engel, T. R. Calhoun, E. L. Read, T.-K. Ahn, T. Mancal, Y.-C. Cheng, R. E. Blankenship, and G. R. Fleming, *Nature (London)* **44**, 782 (2007).

¹²A. Rochefort, P. Boyer, and B. Nacer, *Org. Electron.* **8**, 1 (2007).

¹³L. Li, G. Meller, and H. Kosina, *Microelectron. J.* **38**, 47 (2007).

¹⁴N. Vukmirovic and L. W. Wang, *Phys. Rev. B* **81**, 035210 (2010).

¹⁵M. Barbatti, *WIREs Comp. Mol. Sci.* **1**, 620 (2011).

¹⁶N. L. Doltsinis and D. Marx, *Phys. Rev. Lett.* **88**, 166402 (2002).

¹⁷A. P. Horsfield, D. R. Bowler, A. J. Fisher, T. N. Todorov, and C. G. Sanchez, *J. Phys.: Condens. Matter* **16**, 8251 (2004).

¹⁸M. Born and J. R. Oppenheimer, *Ann. Phys.* **84**, 457 (1927).

¹⁹R. de L. Kronig, *Band Spectra and Molecular Structure* (Cambridge University Press, New York, 1930).

²⁰H. S. W. Massey and R. A. Smith, *Proc. R. Soc. London, Ser. A* **142**, 142 (1933).

²¹J. S. Tse, *Annu. Rev. Phys. Chem.* **53**, 249 (2002).

²²E. J. Heller, *J. Chem. Phys.* **75**, 2923 (1981).

²³G. D. Billing, *Int. Rev. Phys. Chem.* **13**, 309 (1994).

²⁴J. Bedard-Hearn, R. E. Larsen, and B. J. Schwartz, *J. Chem. Phys.* **123**, 234106 (2005).

²⁵J. B. Delos and W. R. Thorson, *Phys. Rev. A* **6**, 720 (1972).

²⁶J. C. Tully, *J. Chem. Phys.* **93**, 1061 (1990).

²⁷J. Y. Fang and S. Hammes-Schiffer, *J. Phys. Chem. A* **103**, 9399 (1999).

²⁸J. E. Subotnik and N. Shenvi, *J. Chem. Phys.* **134**, 024105 (2011).

²⁹F. T. Smith, *Phys. Rev.* **179**, 111 (1969).

³⁰I. N. Ragazos, M. A. Robb, F. Bernardi, and M. Olivucci, *Chem. Phys. Lett.* **197**, 217 (1992).

³¹M. J. Paterson, P. A. Hunt, M. A. Robb, and O. Takahasshi, *J. Phys. Chem. A* **106**, 10494 (2002).

³²M. Ben-Nun, F. Molnar, H. Lu, J. C. Phillips, T. J. Martinez, and K. Schulten, *Faraday Discuss.* **110**, 447 (1998).

³³J. Kiwi and C. Morrison, *J. Phys. Chem.* **88**, 6146 (1984).

³⁴C. J. Smallwood, W. B. Bosma, R. E. Larsen, and B. J. Schwartz, *J. Chem. Phys.* **119**, 11263 (2003).

³⁵R. E. Larsen and B. J. Schwartz, *J. Chem. Phys.* **119**, 7672 (2003).

³⁶S. V. Kilina, D. S. Kilin, and O. V. Prezhdo, *ACS Nano* **3**, 93 (2009).

³⁷C. F. Craig, W. R. Duncan, and O. V. Prezhdo, *Phys. Rev. Lett.* **95**, 163001 (2005).

³⁸S. A. Fischer, W. R. Duncan, and O. V. Prezhdo, *J. Am. Chem. Soc.* **131**, 15483 (2009).

³⁹S. Fernandez-Alberti, V. D. Kleiman, S. Tretiak, and A. E. Roitberg, *J. Phys. Chem. A* **113**, 7535 (2009).

⁴⁰J. Pittner and M. J. Pederzoli, *Phys. Chem. A* **115**, 11136 (2011).

⁴¹T. Nelson, S. Fernandez-Alberti, V. Chernyak, A. E. Roitberg, and S. Tretiak, *J. Phys. Chem. B* **115**, 5402 (2011).

⁴²D. Zanuttini, J. Douady, E. Jacquet, E. Giglio, and B. Gervais, *J. Chem. Phys.* **134**, 044308 (2011).

⁴³I. Tavernelli, B. F. E. Curchod, and U. Roethlisberger, *Chem. Phys.* **391**, 101 (2011).

⁴⁴A. Troisi and G. Orlandi, *Phys. Rev. Lett.* **96**, 086601 (2006).

⁴⁵M. Hultell and S. Stafstrom, *Chem. Phys. Lett.* **428**, 446 (2006).

⁴⁶W. Kohn and L. J. Sham, *Phys. Rev.* **140**, A1133 (1965).

⁴⁷E. Runge and E. K. U. Gross *Phys. Rev. Lett.* **52**, 997 (1984).

⁴⁸J. Li and L. W. Wang, *Phys. Rev. B* **72**, 125325 (2005).

⁴⁹N. Vukmirovic and L. W. Wang, *J. Phys. Chem. B* **113**, 409 (2009).

⁵⁰B. G. Levine, J. D. Coe, A. M. Virshup, and T. J. Martinez, *Chem. Phys.* **347**, 3 (2008).

⁵¹L. W. Wang and A. Zunger, *J. Chem. Phys.* **100**, 2394 (1994).

⁵²N. Vukmirovic and L. W. Wang *J. Chem. Phys.* **134**, 094119 (2011).

⁵³B. L. M. Hendriksen, F. Martin, Y. Qi, C. Mauldin, N. Vukmirovic, J. F. Ren, A. J. Katan, V. Altoe, S. Aloni, J. M. J. Frechet L. W. Wang, and M. Salmeron, *Nano Lett.* **11**, 4107 (2011).

⁵⁴F. Martin, B. L. M. Hendriksen, and M. Salmeron, (unpublished).

⁵⁵J. R. Maple, U. Dinur, and A. Hagler, *Proc. Natl. Acad. Sci.* **85**, 5350 (1988).

⁵⁶L. Verlet, *Phys. Rev.* **159**, 98 (1967).

⁵⁷S. Plimpton, *J. Comp. Phys.* **117**, 1 (1995); <http://lammmps.sandia.gov/>.

⁵⁸J. B. Delos, W. R. Thorson, and S. K. Knudson, *Phys. Rev. A* **6**, 709 (1972).

⁵⁹P. V. Parandekar and J. C. Tully, *J. Chem. Phys.* **122**, 094102 (2005).

⁶⁰E. J. McEniry, Y. Wang, D. Dundas, T. N. Todorov, L. Stella, R. P. Miranda, A. J. Fisher, A. P. Horsfield, C. P. Race, D. R. Mason, W. M. C. Foulkes, and A. P. Sutton, *Eur. Phys. J. B* **77**, 305 (2010).

- ⁶¹N. Suzuki, T. Kawamoto, and M. Shirai, *Mol. Cryst. Liq. Cryst.* **272**, 161 (1995).
- ⁶²D. Jacquemin, B. Champagne, and J.-M. Andre, *J. Chem. Phys.* **108**, 1023 (1998).
- ⁶³J. E. Northrup, *Phys. Rev. B* **76**, 245202 (2007).
- ⁶⁴T. Holstein, *Ann. Phys.* **8**, 325 (1959).
- ⁶⁵M. Lundberg and P. E. M. Siegbahn, *J. Chem. Phys.* **122**, 224103 (2005).
- ⁶⁶H. Geng and L. W. Wang (unpublished).
- ⁶⁷N. Vukmirovic, C. Bruder, and V. M. Stojanovic, *Phys. Rev. Lett.* **109**, 126407 (2012).
- ⁶⁸A. Troisi, *Chem. Soc. Rev.* **40**, 2347 (2011).
- ⁶⁹S. Duhm, Q. Xin, S. Hosoumi, H. Fukagawa, K. Sato, N. Ueno, and S. Kera, *Adv. Mater.* **24**, 901 (2012).
- ⁷⁰H. Yamane, S. Nagamatsu, H. Fukagawa, S. Kera, R. Friedlein, K. K. Okudaira, and N. Ueno, *Phys. Rev. B* **72**, 153412 (2005).
- ⁷¹M. Hultell and S. Stafstrom, *Phys. Rev. B* **75**, 104304 (2007).
- ⁷²B. Kramer and A. MacKinnon, *Rep. Prog. Phys.* **56**, 1469 (1993).
- ⁷³H. Minemawari, T. Yamada, H. Matsui, J. Tsutsumi, S. Haas, R. Chiba, R. Kumai, and T. Hasegawa, *Nature (London)* **475**, 364 (2011).
- ⁷⁴R. A. Marcus, *Rev. Mod. Phys.* **65**, 599 (1993).
- ⁷⁵H. Haken and P. Reineker, *Z. Phys.* **249**, 253 (1972).
- ⁷⁶H. Haken and G. Strobl, *Z. Phys.* **262**, 135 (1973).
- ⁷⁷I. Rips, *Phys. Rev. E* **47**, 67 (1993).
- ⁷⁸V. Kraus and P. Reineker, *Phys. Rev. A* **43**, 4182 (1991).
- ⁷⁹R. Kubo, *Adv. Chem. Phys.* **15**, 101 (1969).
- ⁸⁰V. M. Kenkre and P. Reineker, *Exciton Dynamics in Molecular Crystals and Aggregates* (Springer-Verlag, Berlin, 1982).
- ⁸¹L. Wang, D. Beljonne, L. Chen, and Q. Shi, *J. Chem. Phys.* **134**, 244116 (2011).
- ⁸²J. F. Janak, *Phys. Rev. B* **18**, 7165 (1978).
- ⁸³T. Koopmans, *Physica (Amsterdam)* **1**, 104 (1934).
- ⁸⁴L. W. Wang, *Phys. Rev. B* **82**, 115111 (2010).
- ⁸⁵J. P. Perdew, R. G. Parr, M. Levy, and J. L. Balduz, Jr., *Phys. Rev. Lett.* **49**, 1691 (1982).
- ⁸⁶A. J. Cohen, P. Mori-Sanchez, and W. Yang, *Science* **8**, 792 (2008).
- ⁸⁷L. Hedin, *Phys. Rev.* **139**, A796 (1965).
- ⁸⁸F. Bruneval, *Phys. Rev. Lett.* **103**, 176403 (2009).
- ⁸⁹B. Lee, L. W. Wang, C. D. Sparatu, and S. G. Louie, *Phys. Rev. B* **76**, 245114 (2007).
- ⁹⁰L. W. Wang, *J. Phys. Chem. B* **109**, 23330 (2005).
- ⁹¹G. Zhang, A. Canning, N. Gronbeck-Jensen, S. Derenzo, and L. W. Wang, *Phys. Rev. Lett.* **110**, 166404 (2013).
- ⁹²D. R. Hamann, M. Schluter, and C. Chiang, *Phys. Rev. Lett.* **43**, 1494 (1979).